

# Edge turbulence measurements in electron-heated Helically Symmetric Experiment plasmas

W. Guttenfelder,<sup>1,a)</sup> D. T. Anderson,<sup>1</sup> F. S. B. Anderson,<sup>1</sup> J. M. Canik,<sup>2</sup> K. M. Likin,<sup>1</sup> and J. N. Talmadge<sup>1</sup>

<sup>1</sup>Department of Electrical and Computer Engineering, University of Wisconsin-Madison, Madison, Wisconsin 53706, USA

<sup>2</sup>Oak Ridge National Laboratory, Oak Ridge, Tennessee 37831, USA

(Received 24 April 2009; accepted 27 July 2009; published online 20 August 2009)

This paper presents edge measurements utilizing Langmuir probes to characterize plasma turbulence in the Helically Symmetric Experiment (HSX) [F. S. B. Anderson *et al.*, *Fusion Technol.* **27**, 273 (1995)]. Normalized density and potential fluctuations exhibit strong intensities but are comparable to mixing length estimates using measured correlation lengths. The correlation lengths are isotropic with respect to radial and poloidal directions and follow local (gyro-Bohm) drift wave expectations. These observations are common to measurements in both the optimized quasihelically symmetric (QHS) configuration, as well as a configuration where the symmetry is degraded intentionally. The resulting turbulent particle flux in higher density QHS discharges is in good quantitative agreement with transport analysis using three-dimensional neutral gas simulations. The measured turbulence characteristics are compared to a quasilinear trapped electron mode (TEM) drift wave model [H. Nordman, J. Weiland, and A. Jarmén, *Nucl. Fusion* **30**, 983 (1990)] that has been used to predict the anomalous transport in HSX. While quantitative differences exist (factors of 2–3), there is a general consistency between the turbulence measurements and the TEM drift wave model. © 2009 American Institute of Physics. [DOI: [10.1063/1.3205884](https://doi.org/10.1063/1.3205884)]

## I. INTRODUCTION AND BACKGROUND

In both tokamaks and stellarators the global energy confinement is dominated by mechanisms other than neoclassical (collisional) transport.<sup>1–4</sup> In most cases, the anomalous transport is a result of turbulence arising from microinstabilities driven by gradients in the plasma density and temperature. In some tokamak cases,<sup>5</sup> large scale, nonlinear gyrokinetic simulations are now capable of quantitative predictions that agree with experimental transport within uncertainties. Because of the computational expense involved in such detailed calculations, the number of “successful” direct comparisons is quite limited. Alternatively, faster reduced transport models<sup>6–9</sup> based on the more comprehensive simulations have also been used to predict temperature profiles and energy confinement times for a variety of tokamak discharges.<sup>1</sup>

In addition to predicting transport, the large scale turbulence simulations, and reduced transport models based on them, make predictions for the “intermediate” quantities, such as the fluctuation intensity, wavenumber spectra, cross phases (e.g., density-potential), and correlation lengths. In an effort to thoroughly validate theory and modeling,<sup>10</sup> as many of these intermediate turbulence quantities that can be measured should be compared to model predictions, concurrent with the transport comparison. Recently, there has been increased focus on making such broad-ranging comparisons in tokamaks.<sup>11–13</sup> In this paper, we will make comparisons of calculations of turbulent transport, as well as the intermediate quantities, to experimental measurements in a stellarator.

Stellarators offer inherent advantages for fusion reactors as they do not require internal plasma currents. However, the increased complexity in geometry complicates both experimental and theoretical analyses. The lack of symmetry also leads to increased neoclassical transport, flow damping, and direct loss of energetic particle (e.g., fusion alphas). However, as the confining field is created by external coils, stellarators offer the flexibility to optimize the magnetic field based on a variety of criteria. As a result, modern stellarators are routinely optimized based on the theoretical understanding of neoclassical theory.<sup>14</sup>

One such device, the Helically Symmetric Experiment (HSX) stellarator<sup>15</sup> was optimized to be quasihelically symmetric (QHS),<sup>16</sup> i.e., the magnetic field strength within a flux surface is symmetric in a helical angle. Experiments in HSX have verified the reduction in flow damping,<sup>17</sup> energetic particle losses,<sup>18</sup> and thermal transport<sup>19</sup> consistent with expectations from neoclassical theory. In particular, the neoclassical transport is reduced to such small values that the resulting particle and electron heat transport in electron cyclotron resonance heated (ECRH) plasmas are anomalous over most of the minor radius. Based on the success of the neoclassical optimizations in HSX and other stellarators<sup>20,21</sup> there is an emerging emphasis on understanding, and hopefully predicting, the turbulence and anomalous transport in stellarators so future experiments may be optimized based on minimizing both neoclassical and turbulent transport.

Linear and nonlinear three-dimensional (3D) gyrokinetic simulations performed for many stellarator configurations<sup>22–28</sup> demonstrate that they are susceptible to the same type of drift wave microinstabilities present in tokamaks, in-

<sup>a)</sup>Present address: Department of Physics, University of Warwick, CV4 7AL, UK. Electronic mail: [w.guttenfelder@warwick.ac.uk](mailto:w.guttenfelder@warwick.ac.uk).

cluding ion temperature gradient (ITG), trapped electron mode (TEM), and electron temperature gradient (ETG). Recently, a modified version of the Weiland ITG/TEM model<sup>6,7</sup> was used to model the anomalous transport in HSX.<sup>28</sup> The results suggest that the anomalous transport in HSX can be explained by TEM transport driven by both electron temperature and density gradients in the helically symmetric geometry. It is natural to question whether the measured turbulence is consistent with this model prediction, or if the transport prediction is simply fortuitous. In this paper, we present measurements using Langmuir probes to diagnose the edge turbulence in HSX to determine (1) if the turbulence characteristics are consistent with the expectations from TEM drift waves, and (2) if the resulting turbulent transport can indeed account for the anomalous transport inferred from one-dimensional (1D) transport analysis. While there are some quantitative differences between the TEM model predictions and the turbulence measurements, there is a general qualitative consistency that supports the explanation of anomalous transport in HSX.

The remainder of this paper is structured as follows. In Sec. II, experimental details, including the Langmuir probes utilized, are discussed. Section III presents the turbulence measurements and analysis. Section IV will show and discuss the direct comparison of the analyzed measurements with the Weiland TEM model. The results will be summarized in Sec. V.

## II. EXPERIMENTAL BACKGROUND AND MEASUREMENT DETAILS

HSX is a four field period device with average major and minor radii of  $\langle R \rangle = 1.2$  m and  $\langle a \rangle = 12$  cm, respectively. The main magnetic field is produced by 48 external modular coils. Using a spectral representation, the magnetic field on a flux surface labeled by  $\rho$  can be written as

$$B(\rho, \theta, \phi)/B_0(\rho) = \sum_{n,m} b_{n,m}(\rho) \cos(n\phi - m\theta). \quad (1)$$

The magnetic field ripple in the QHS configuration is dominated by the helical  $[n,m]=[4,1]$  component, i.e.,

$$B(\rho, \theta, \phi)/B_0(\rho) \approx 1 - |b_{41}| \cos(4\phi - \theta). \quad (2)$$

The magnitude of this component is approximately  $|b_{41}| \approx 0.14r/a$ , where  $r/a$  is the normalized minor radius defined using the toroidal flux  $\Psi$ ,  $\rho = r/a = \sqrt{\psi/\psi_{LCFS}}$  (LCFS is the last closed flux surface). Additional nonsymmetric ( $n/m \neq 4$ ) components exist, but at much smaller amplitudes (less than 1%).

Surrounding each main coil is a separate planar coil. These auxiliary coils can be energized in a fashion that intentionally degrades the quasihelical symmetry. For some of the measurements presented in this paper, these coils have been used to introduce a dominant toroidal mirror ripple  $[n,m]=[4,0]$ , with a magnitude  $b_{40} \approx 0.08$  roughly independent of minor radius. The nonsymmetric ripple increases neoclassical transport toward the level of a conventional stellarator allowing for comparisons between optimized and

nonoptimized configurations within the same device. This particular “Mirror” configuration is the same as that used in the experiments reported in Refs. 17 and 29.

The plasmas investigated here were heated by second harmonic X-mode electron cyclotron resonance heating (ECRH) ( $B=0.5$  T, 28 GHz gyrotron) with a nominal 50 kW of injected power. Peak electron temperatures measured via the Thomson scattering<sup>30</sup> reach 500 eV or larger for central line-averaged densities (measured with microwave interferometry<sup>31</sup>) of  $(1-2) \times 10^{12}$  cm<sup>-3</sup>. Ion temperatures measured by impurity Doppler spectroscopy are  $T_i \approx 20$  eV.<sup>17</sup> While an ion temperature profile measurement is not available, the balance of collisional electron-ion energy exchange with ion-neutral charge exchange is consistent with negligible ion transport, hence little expected ITG. The electron temperature and density place the electrons deep in the long mean free path regime across the entire minor radius. As a result, the TEM is the expected theoretical drift wave instability,<sup>28</sup> even near the edge where the measurements described in this paper were performed. The ETG instability is expected to be unstable in some cases near the core, but theoretically cannot account for the anomalous particle transport.

Figure 1 illustrates two probe configurations constructed to diagnose the edge plasma in HSX. While both probes are mounted on the *outboard* side of the machine ( $\theta$  near zero), they are mounted at toroidal angles offset by roughly one half field period ( $\phi$  near 0 and  $\pi/4$ ). As a result of the helical symmetry [Eq. (2)], the low field side (LFS) probe [Fig. 1(a)] is near minimum  $B$  on a flux surface, while the high field side (HFS) probe [Fig. 1(b)] is close to a maximum. Correspondingly, the LFS probe is near the center of trapped particle orbits, while the HFS probe only samples barely trapped particles. In addition, the curvature and grad-B drifts within a flux surface (proportional to  $\vec{\kappa} \cdot \nabla \psi$  and  $\nabla B \cdot \nabla \psi$ ) are of opposite sign at these two locations. The LFS probe is therefore in a region of local “bad” curvature, i.e., unstable to ballooninglike perturbations, similar to the outboard side of a tokamak. The HFS probe is in a region of “good” curvature, similar to the inboard side of a tokamak. It might therefore be expected that these two regions should theoretically exhibit different local stability properties.

Figure 1 also shows the cross section of the flux surfaces (determined from vacuum field line integration) at the toroidal locations where the probes are mounted. The shaping at these two locations is significantly different. The distance between the LCFS and the magnetic axis is about  $\sim 7$  cm for the LFS probe and over 20 cm for the HFS probe.

Each probe head utilizes four tungsten tips ( $d_p = 0.74$  mm diameter, 3 mm exposed) in boron nitride (12.6 mm diameter), with a separation of 3.2 mm between each tip. Three tips are aligned to sample the same flux surface while the fourth tip is recessed an additional 6.4 mm. The probe tips are aligned to be perpendicular to the local magnetic field.

To measure time-resolved fluctuations, the probe tips are electrically configured to measure either floating potential or ion saturation current. The floating potential is measured across a 1 M $\Omega$  resistance inserted between the probe tip and

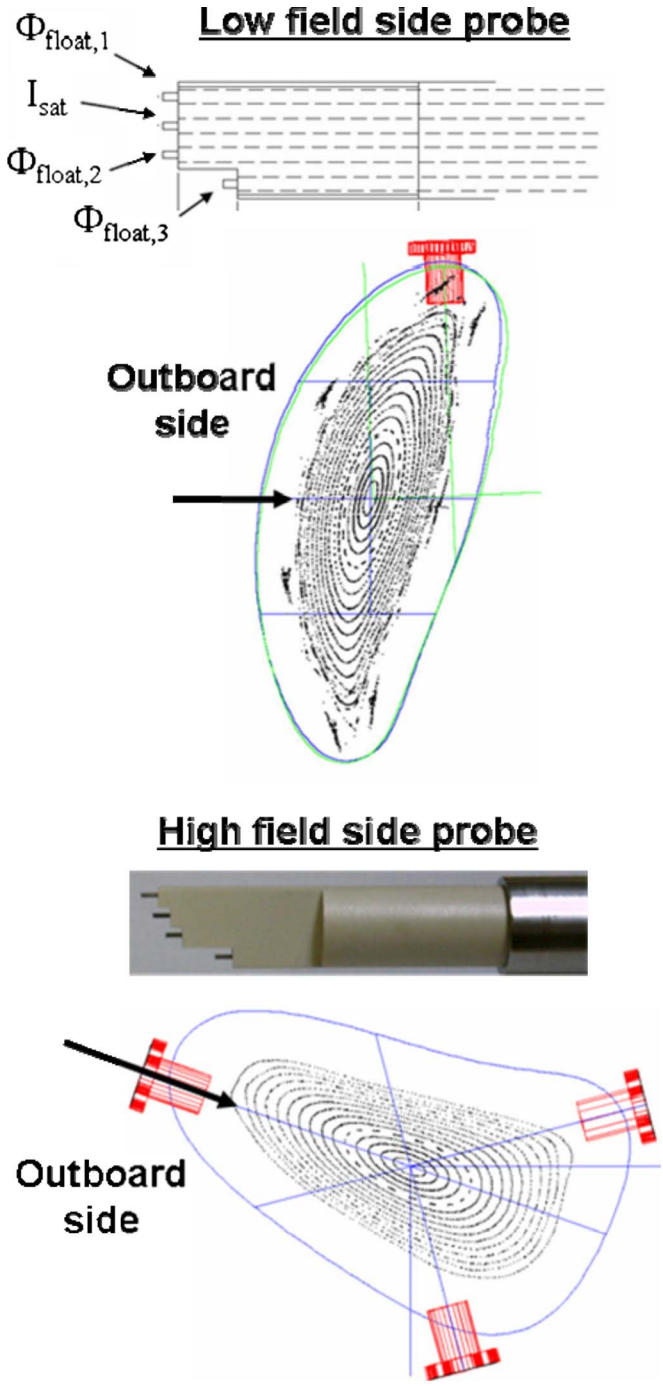


FIG. 1. (Color online) Probe configurations used for the turbulence measurements at two different toroidal locations,  $\phi \approx 0$  and  $\phi \approx \pi/4$ . A poloidal cut of the QHS flux surfaces is also shown for each location.

the plasma vessel. Ideally it differs from the plasma potential by a drop across the probe sheath, given by  $\Phi_{\text{plasma}} = \Phi_{\text{float}} + \mu T_e$ , where  $\mu$  depends on the ratio of electron to ion mass (electron temperature fluctuations have not been measured in this work and are neglected) for  $T_e > T_i$  and unmagnetized hydrogen ions ( $\rho_i \approx 1.5$  mm  $> r_p = 0.37$  mm),  $\mu = 0.5 \ln(0.36m_i/2\pi m_e) \approx 3.3$ .<sup>32</sup> This also relies on the assumption of a planar probe surface, which is reasonable since the Debye length ( $\sim 70 \mu\text{m}$ ) is much smaller than the tip diameter. The ion saturation current provides a simple measure of the local plasma density,  $I_{\text{sat}} \approx 0.6 \text{enc}_s A_c$ , where  $A_c$  is

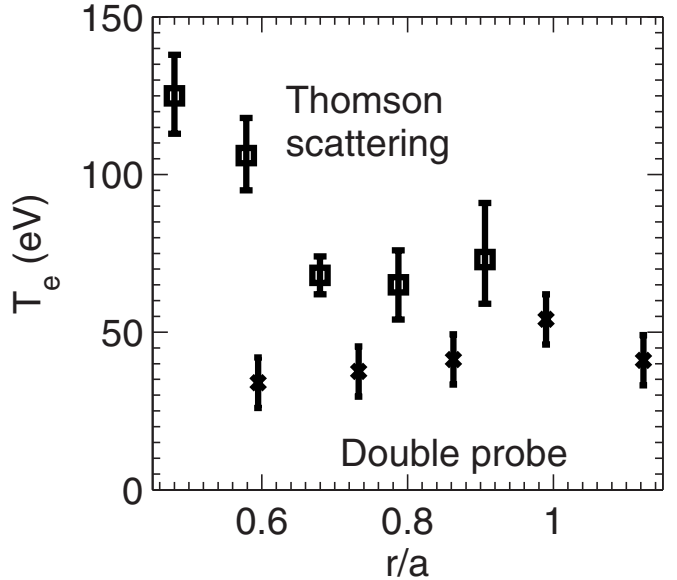


FIG. 2. Edge electron temperatures measured by the Thomson scattering (squares) and a double probe (crosses) for a 0.5 T QHS plasma ( $\langle n_e \rangle = 1.0 \times 10^{12} \text{ cm}^{-3}$ ).

the collection area of the probe tip and  $c_s$  is the local sound speed [ $c_s = (T_e/m_i)^{1/2}$ ]. It is determined by applying a large negative potential (-300 V) to the probe tip and measuring the voltage drop across a small series resistance (a few ohms). The signals are acquired by high bandwidth optically isolated amplifiers (four pole filter, cutoff frequency  $\approx 1$  MHz) and digitized at 5 MHz.

Two of the three tips aligned on a flux surface are configured to measure floating potential so the poloidal electric field fluctuations [ $E_\theta = (\Phi_{\text{float},1} - \Phi_{\text{float},2})/d_\theta$ ], and hence radial  $E \times B$  velocities can be inferred. Here  $d_\theta = 6.4$  mm is the separation between the two tips. The probe tip between the two tips that measure floating potential is configured to measure the ion saturation current (Fig. 1). Correlation analysis can be used to determine the density-potential cross phase from these three signals, as well as the inferred local turbulent driven radial particle flux. The fourth recessed probe tip measures floating potential, which is used to determine the local radial electric field and the radial correlation length of the turbulence. Additional measurements with the probe head rotated 180° were acquired to ensure shadowing effects did not modify interpretation of the recessed probe tip data.

The probes were moved on a shot-by-shot basis to create radial profiles. In  $B=0.5$  T plasmas, probes could be inserted as far as  $\rho = r/a \approx 0.6$  while maintaining density control. However, as the probes are moved inside  $r/a \approx 0.8$ , the total stored energy (measured by a diamagnetic flux loop) begins to decrease, dropping a total of  $\sim 20\%$  (from 22 to 17 J) by  $r/a = 0.6$ . Figure 2 shows the edge radial electron temperature profile measured by the Thomson scattering in the absence of probes, and by the LFS probe configured as a swept double probe.<sup>32</sup> A drop in the local electron temperature is noticeable as the probe assembly is inserted further into the plasma. Therefore most measurements reported were acquired near or outside  $r/a \approx 0.8$ .

It is important to note that while the local electron tem-

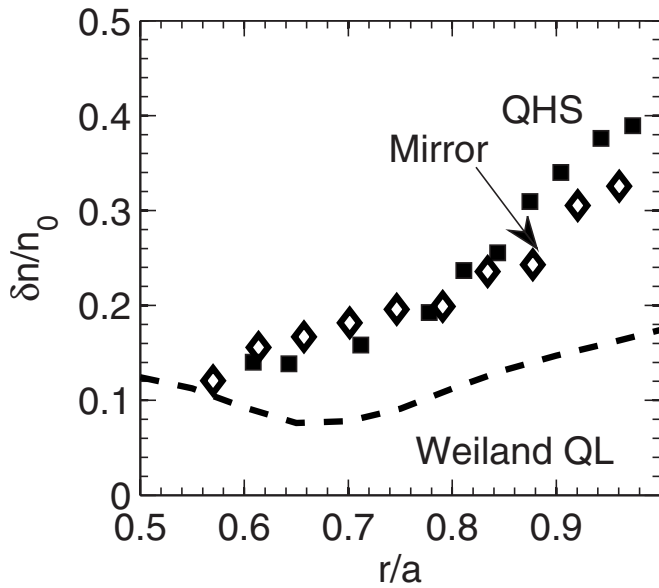


FIG. 3. Normalized  $I_{\text{sat}}$  fluctuation levels measured in both the QHS and Mirror configurations. Also shown is the mixing length estimate used in the Weiland model.

perature gradient may be relatively small in the edge with the diagnostic probes inserted, a strong density gradient ( $a/L_p \approx 2-3$ ) remains that is capable of destabilizing the TEM,<sup>28</sup> which can drive the resulting turbulence and transport.

### III. TURBULENCE CHARACTERISTICS

#### A. Fluctuation intensity, length, and time scales

Time series of ion saturation current and floating potential have been measured in both QHS and Mirror plasmas. Figure 3 shows the radial profiles of the corresponding  $I_{\text{sat}}$  fluctuation levels (standard deviation from the time average), normalized to the time-averaged values, for both QHS and Mirror configurations at a line-averaged density of  $\langle n_e \rangle = 1.0 \times 10^{12} \text{ cm}^{-3}$ . The fluctuation levels range between 10%–40% for the location of  $r/a \approx 0.6$ –1.0, and are similar in both configurations. The fluctuation levels of the floating potential measurements are 10–16 V in amplitude inside the separatrix, corresponding to relative values of 25%–40% when normalized to the electron temperatures measured by the double probe in Fig. 2. These values are very similar to the normalized  $I_{\text{sat}}$  fluctuation levels, consistent with expectations from linear electron drift wave theory ( $\delta n/n_0 \sim e \delta \Phi / T_e$ ).

While these normalized fluctuation levels are relatively large compared to “typical” core values (few percent) in magnetic confinement devices,<sup>33–35</sup> they are consistent with mixing length estimates based on a radial correlation length of the order  $\sim \rho_s$ , where  $\rho_s = c_s / \Omega_i$ ,  $c_s = (eT_e/m_i)^{1/2}$ , and  $\Omega_i = eB/m_i$ . A simple mixing length estimate can be derived under the assumption that the instantaneous gradient ( $k_r \delta n$ ) is limited in magnitude to the background equilibrium gradient ( $\nabla n_0$ ). This leads to  $\delta n/n_0 \approx L_r/L_n$ , where  $L_n = -\nabla n_0/n_0$  and  $L_r$  represents an average radial correlation length ( $L_r \sim k_r^{-1}$ ). In Fig. 2, at  $r/a=0.8$ ,  $\delta n/n_0 \approx 25\% \approx 8\rho_s/L_n$ , sug-

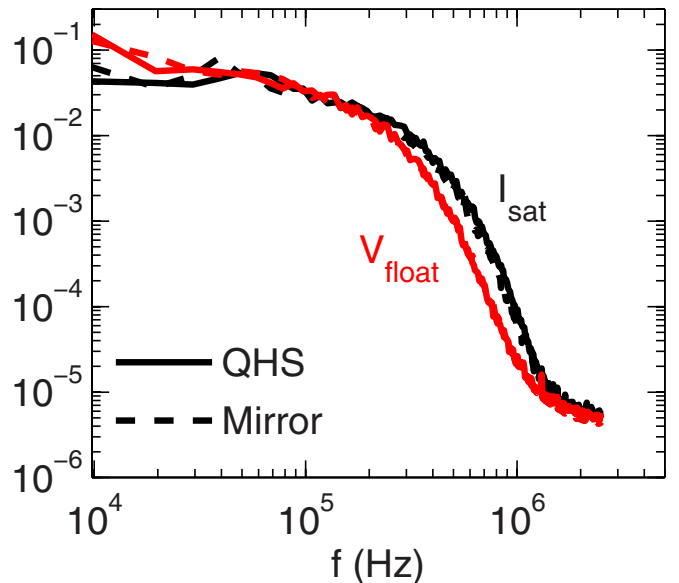


FIG. 4. (Color online) Power spectra of  $I_{\text{sat}}$  and  $V_{\text{float}}$  at  $r/a=0.8$  for both QHS and Mirror configurations.

gesting a radial correlation length of about  $L_r \approx 8\rho_s$  ( $\sim 1$  cm), similar to measurements in other devices.<sup>33–35</sup>

Fourier transforms have been used to characterize the frequency content of the fluctuations. To create statistically meaningful spectra, time series (10–40 ms of stationary data) are separated into 100  $\mu\text{s}$  segments, limiting the frequency resolution to 10 kHz. Spectra are calculated for each of the 100–400 realizations and averaged together, reducing the uncertainty in the expected value of any frequency to 5%–10% ( $1/\sqrt{N}$ ). The resulting power spectra, normalized by the variance of each signal, are shown in Fig. 4 for both  $I_{\text{sat}}$  and  $V_{\text{float}}$  at  $r/a=0.8$ . The fluctuations exist over a broad range of frequencies, up to 100–300 kHz, before decaying rapidly with a spectral index ( $P \sim f^{-m}$ ) of about  $m=4$ . Furthermore, the frequency content in each configuration is nearly identical. Assuming drift waves are present, they should have characteristic frequencies of  $\omega_{*e}/2\pi \sim k_\theta T_e/BL_n 2\pi \sim 20$ –100 kHz (assuming  $k_\theta \rho_s = 0.1$ –0.5), similar to the range of frequencies measured. However, the frequencies measured in the laboratory frame of reference will include a Doppler shift due to equilibrium  $E \times B$  velocities ( $\omega_{\text{lab}} = \omega_{*e} + k_\theta V_{E \times B}$ ). The impact of this Doppler shift will be discussed later.

Correlation analysis can be used with multiple probe tips to characterize the spatial scales of the fluctuations. An estimate of the local poloidal wavenumber,<sup>36</sup> at a given frequency, is made by using the cross phase calculated between the Fourier spectra of two probe tip measurements,  $F_\Phi(f)$ ,

$$k_\theta(f) = \frac{1}{d_\theta} \text{phase}[F_{\Phi 1}^*(f) F_{\Phi 2}(f)], \quad (3)$$

separated by a distance  $d_\theta$ . From the numerous time series realizations, a local poloidal wavenumber-frequency spectra  $S_L(k_\theta, \omega)$  is calculated.<sup>36</sup> This local  $k_\theta f$  spectrum provides an estimate of the spatial scales present in the fluctuations at a given frequency. Figure 5 shows a contour plot of the magnitude of the local  $k_\theta f$  spectra for the QHS  $r/a=0.8$  data for

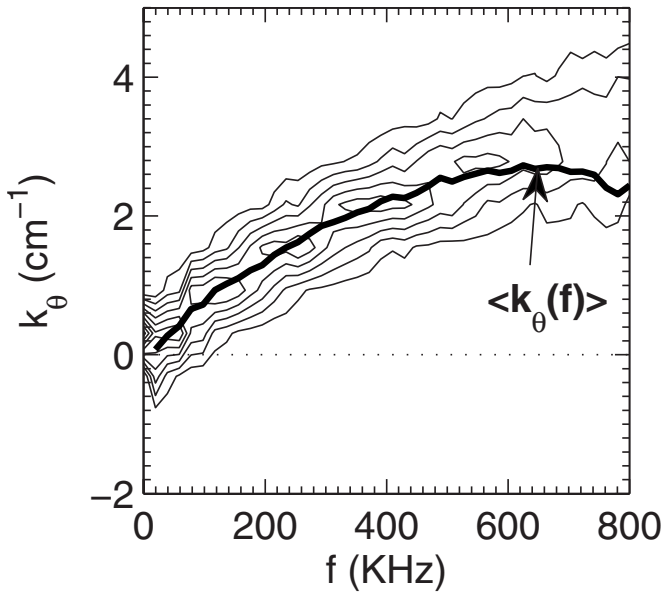


FIG. 5. Local  $k_\theta$ - $f$  spectra (conditioned on the fluctuation amplitude at each frequency) for the QHS configuration at  $r/a=0.8$ . The bold solid line is the average poloidal wavenumber at each frequency  $\langle k_\theta(f) \rangle$ .

$\langle n_e \rangle = 1.0 \times 10^{12} \text{ cm}^{-3}$ . The amplitude at each frequency has been normalized to the total fluctuation level at that frequency [i.e.,  $S_L(k_\theta, \omega)/S(\omega)$ ]. While the fluctuations are spread over many wavenumbers, a clear dispersion is observed, as indicated by the mean wavenumber  $\langle k_\theta(f) \rangle$  (solid line). A phase velocity is estimated using the most intense fluctuations ( $f < 100$  kHz, Fig. 4) to be  $V_{\text{phase}} = \omega/k_\theta \approx 2\pi 10^5 \text{ s}^{-1}/100 \text{ m}^{-1} \approx 6 \text{ km/s}$ .

A local poloidal wavenumber spectrum can be estimated by integrating the local  $k_\theta$ - $f$  spectra over frequency,  $S_L(k_\theta) = \int_f S_L(k_\theta, f) df$ . Figure 6 shows the local  $k_\theta$  spectra calculated for the same condition as Fig. 5. The spectra are very similar between the two configurations, with mean wave-

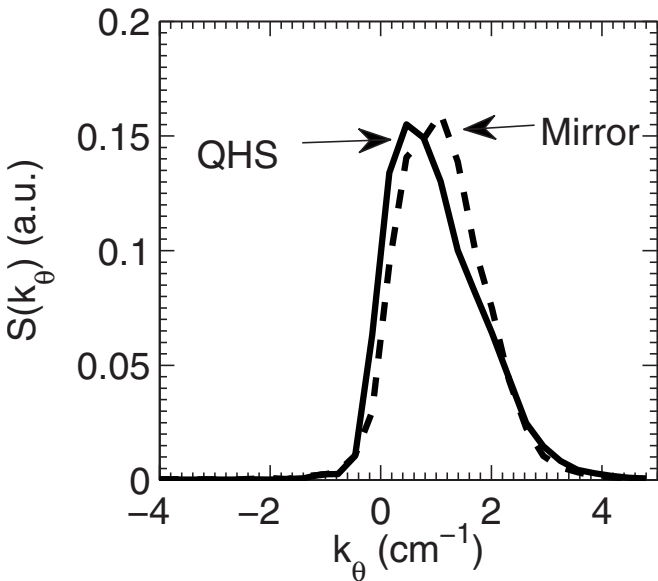


FIG. 6. Local poloidal wavenumber spectra for the QHS and Mirror configurations for the same conditions as Fig. 5.

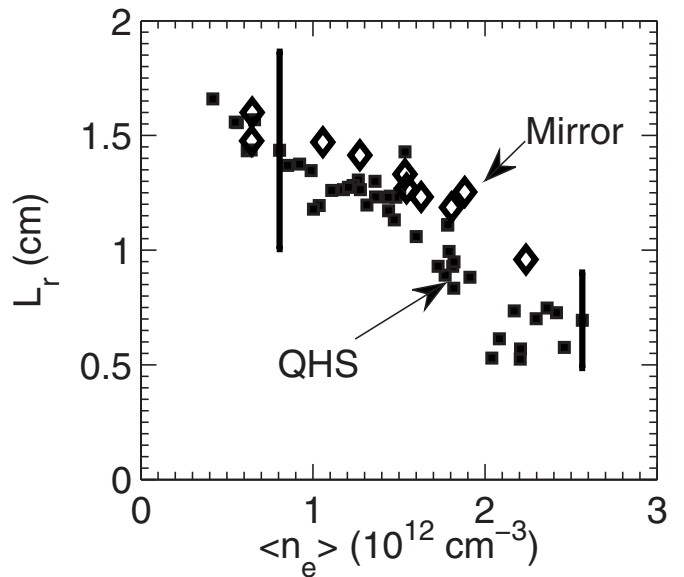


FIG. 7. Radial correlation lengths vs line-averaged density at  $r/a=0.8$  for QHS and Mirror configurations.

numbers of  $\langle k_\theta \rangle \approx 1.0$  and  $1.1 \text{ cm}^{-1}$  for QHS and Mirror, respectively. Using the electron temperature of  $T_e = 40 \text{ eV}$  ( $\rho_s \approx 0.13 \text{ cm}$ ),  $\langle k_\theta \rangle \rho_s \approx 0.14$ , comparable to other experimental results.<sup>33–35</sup> The standard deviation of  $k_\theta$  ( $\Delta k_\theta = \langle (k_\theta - \langle k_\theta \rangle)^2 \rangle^{1/2}$ ) is slightly smaller than the mean value in each case. Assuming a Gaussian spectrum shape, the corresponding poloidal correlation length (half width at half maximum) would be  $L_\theta \approx 1.2/\Delta k_\theta \approx 7–8\rho_s$ , very similar to the estimated radial correlation length derived from the fluctuation levels and mixing length estimate discussed above.

A radial correlation length,  $L_r$ , is found more directly by using the cross correlation,  $C(\Delta r, \Delta t)$ , between two radially separated ( $\Delta r$ ) measurements, via

$$C_{\max}(\Delta r, \Delta t) \approx \exp(-\Delta r/L_r) \Rightarrow L_r = \frac{-\Delta r}{\ln(C_{\max})}. \quad (4)$$

This analysis has been performed using the additional floating potential measurement from the radially recessed probe tip (Fig. 1). Although this tip is also separated poloidally from its nearest neighbor, both the cross correlation and coherence are much larger between poloidally separated tips compared to the radially separated tips. Therefore the above approximation is reasonable.

Figure 7 shows the radial correlation lengths calculated with Eq. (4) (at  $r/a=0.8$ ) for density scans in both the QHS and Mirror configurations. Again, the correlation lengths are very similar between configurations for the same line-average density. As the density is increased, the radial correlation length decreases from  $\sim 0.5$  to  $\sim 0.1$  cm. A comparable decrease in the characteristic poloidal scale length ( $\sim \Delta k_\theta^{-1}$ ) is also observed for this density scan. The relative uncertainty results mostly from the finite sampling length of the probe tips (3 mm length) compared to their separation (6.4 mm).

For a similar scan in density, the double probe measurements indicate that the local  $T_e$  (at  $r/a=0.8$ ) decreases from 50 to 30 eV between the densities of  $(0.5\text{--}1.5) \times 10^{12} \text{ cm}^{-3}$ . This reduction in temperature corresponds to a reduction in  $\rho_s (\sim T_e^{1/2})$  of  $\sim 20\%$  (1.4–1.1 mm). In this range of densities, the correlation lengths also decrease  $\sim 30\%$ , from 1.5 to 1.0 cm. The radial and poloidal correlation lengths remain isotropic and are almost linearly proportional to the local value of  $\rho_s$  ( $\langle \Delta k_\theta \rangle^{-1} \sim L_r \sim 7\rho_s$ ), as expected from gyro-Bohm scaling inherent to local drift wave theory.

As electron drift waves are expected to be dominant in these ECRH plasmas in HSX, the turbulent fluctuations (in the plasma frame of reference) are theoretically expected to propagate in the electron diamagnetic drift direction. However, as mentioned previously, the measurements in the laboratory frame of reference are Doppler shifted by the local equilibrium  $E \times B$  velocity. In an attempt to extract the mode velocity of the drift waves, both the phase velocity of the fluctuations (in the laboratory frame of reference) and the radial electric field need to be measured.

The phase velocity can be inferred from the local  $k_\theta f$  spectra discussed earlier. As shown in Fig. 5, there is strong correlation between the measured poloidal wavenumber and frequency. For the broad turbulent spectrum in Fig. 5, a phase velocity can also be calculated using a spectrum average,<sup>37</sup>

$$V_{\text{phase}} = \frac{\int_{k_\theta, \omega} \left( \frac{\omega}{k_\theta} \right) S_L(k_\theta, \omega) dk_\theta d\omega}{\int_{k_\theta, \omega} S_L(k_\theta, \omega) dk_\theta d\omega}. \quad (5)$$

For the data in Fig. 5, the spectrum-averaged phase velocity is calculated to be 7.0 km/s in the ion diamagnetic drift direction. This is similar to the value determined from the simple estimate (6 km/s) discussed above.

The phase velocity of the measured fluctuations calculated for the QHS density scan of Fig. 7 is shown in Fig. 8. Also shown are the  $E \times B$  drift velocities calculated using the time-averaged values of the radially separated floating potential measurements. There is a strong correlation between the  $E \times B$  velocity and the measured phase velocities. They both propagate in the ion (electron) diamagnetic direction at low (high) density.

From this figure, the inferred mode velocities ( $V_{\text{mode}} = V_{\text{phase}} - V_{E \times B}$ ) are nearly always in the ion diamagnetic drift direction, contrary to the expectation for electron drift waves. However, to determine the correct  $E \times B$  drift velocity from the floating potential measurements requires a correction due to the local electron temperature gradient ( $-\mu \nabla T_e$ ) which was not included in Fig. 8. It is unclear what the appropriate temperature gradient is at the location of the probe measurements, especially considering the perturbative nature of the probe measurements. While there is scatter in the data, the Thomson scattering measurements in Fig. 2 (in the absence of probes) illustrate  $T_e$  decreases from  $\sim 120$  eV ( $r/a=0.5$ ) to 60 eV ( $r/a=0.9$ ), corresponding to a gradient of  $-\nabla T_e/e \sim 20$  V/cm. Using  $\mu=3$ , this amounts to an in-

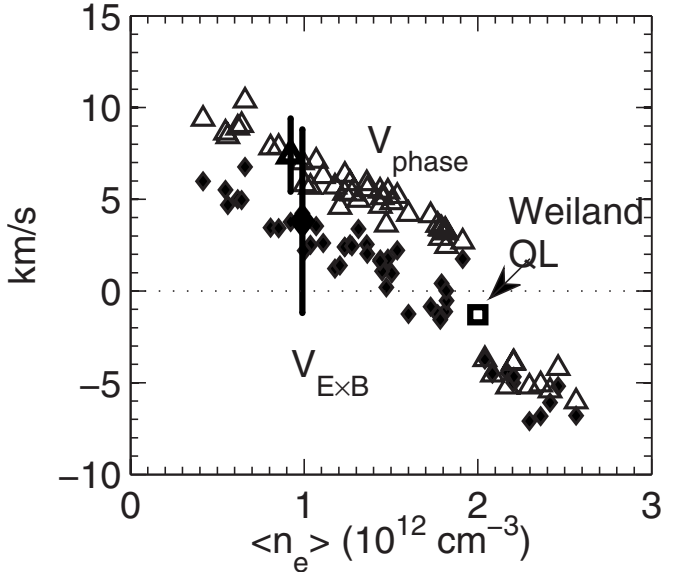


FIG. 8. Spectrum averaged phase velocities for the QHS density scan data (triangles), local  $E \times B$  velocity determined by the radially separated floating potential measurements (diamonds), and mode velocity from the Weiland model (square).

crease in  $V_{E \times B}$  of about 12 km/s over the  $V_{E \times B} \sim 4$  km/s from the floating potential measurements, for a total  $V_{E \times B} \approx 16$  km/s at  $\langle n_e \rangle = 1.0 \times 10^{12} \text{ cm}^{-3}$ . This would be consistent with phase velocities in the electron diamagnetic direction when the phase velocity is only 7 km/s. However, the double probe measurements in Fig. 2 indicate a near zero or reversed  $T_e$  gradient implying mode velocities remain propagating in the ion diamagnetic drift direction. The error bar on the  $E \times B$  velocity in Fig. 8 represents this uncertainty in the local electron temperature gradient, which prevents direct confirmation of the mode propagation direction.

## B. Turbulent particle transport

Using the Fourier spectra of the floating potential and ion saturation current measurements, a local density-potential cross phase spectra,  $\alpha_{n\Phi}(f)$ , can be calculated,

$$\alpha_{n\Phi}(f) = \text{phase}[F_n^* F_\Phi]. \quad (6)$$

In practice, this is determined by averaging the two  $I_{\text{sat}} \cdot \Phi_{\text{float}}$  cross phase spectra determined independently using the  $\Phi_{\text{float}}$  measurements on either side of the  $I_{\text{sat}}$  measurement (Fig. 1). It is important to use this average, as the separation between the probe tips (0.32 cm) is a significant fraction of the characteristic poloidal scale length ( $\sim 1$  cm). Using only one  $V_{\text{float}}$  measurement artificially biases the cross phase measurement, depending on the direction of the phase velocity.

With the above  $n\varphi$  cross phase spectra, and the local poloidal wavenumber spectra  $k_\theta(f)$  calculated previously, it is possible to estimate the turbulent driven particle flux spectra,<sup>38</sup>

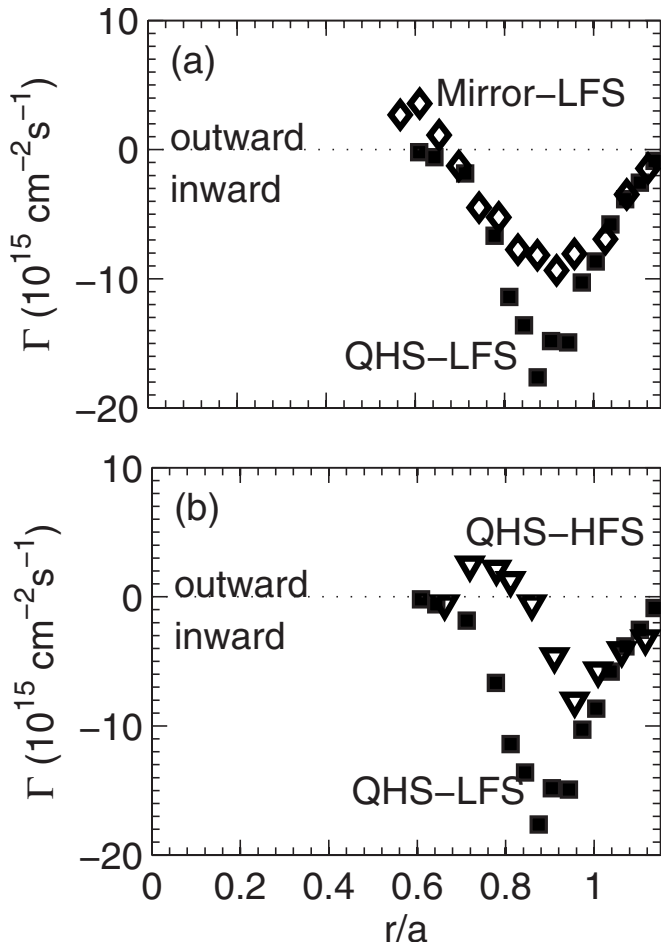


FIG. 9. (a) Turbulent driven particle flux at  $\langle n_e \rangle = 1 \times 10^{12} \text{ cm}^{-3}$  for QHS and Mirror plasmas, measured with the LFS probe. (b) Turbulent driven particle fluxes from both LFS and HFS probes in the QHS configuration.

$$\begin{aligned}\Gamma(f) &= \text{Re}\{-ik_\theta(f)F_n^*(f)F_\varphi(f)\}/B, \\ \Gamma(f) &= \text{Im}\{k_\theta(f)F_n^*(f)F_\varphi(f)\}/B, \\ \Gamma(f) &= k_\theta(f)|P_{n\Phi}(f)|\sin[\alpha_{n\Phi}(f)]/B,\end{aligned}\quad (7)$$

where  $|P_{n\Phi}(f)|$  is the amplitude of the density-potential cross spectrum. Figure 9(a) shows the radial profiles of the spectrally averaged turbulent particle flux ( $\int_f \Gamma(f) df$ ) at  $\langle n_e \rangle = 1 \times 10^{12} \text{ cm}^{-3}$  for QHS and Mirror plasmas. The resulting fluxes are of comparable magnitude to the fluxes determined using absolutely calibrated  $H_\alpha$  emission measurements coupled with 3D DEGAS (Ref. 39) neutral gas simulations (described in Ref. 19). However, the turbulent driven fluxes for these two plasmas are measured to be directed inwards, up the density gradient.

There is no reason to assume the turbulent particle flux is symmetric on a flux surface, especially in highly shaped plasmas such as those in HSX. Therefore, the turbulent particle flux was also measured using the HFS probe. Figure 9(b) shows that the turbulent particle flux measured in this second location with different local geometries is also directed inward in the region  $r/a > 0.85$ .

It is unclear why the measured transport is directed inward for these plasmas. However, as the line-averaged den-

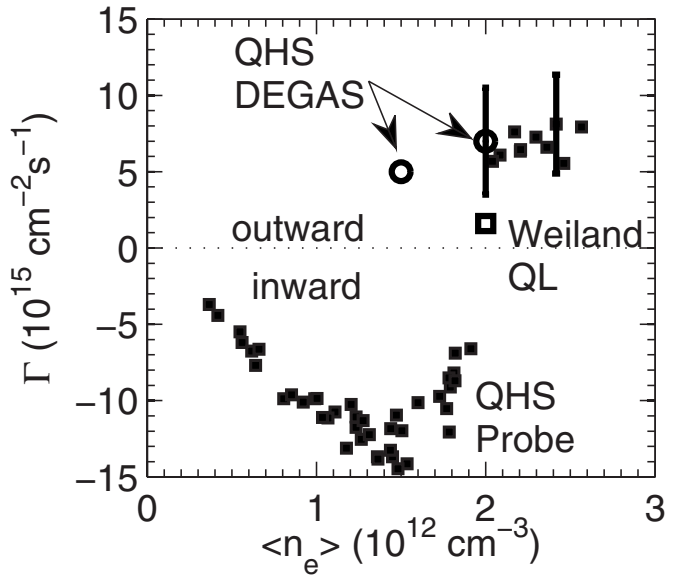


FIG. 10. Measured turbulent particle flux from the LFS probe ( $r/a=0.8$ ) for the QHS density scans (closed squares). Also shown are values determined from 3D DEGAS simulations (circles) and predicted from the Weiland model (open square).

sity is increased, the direction of the measured transport changes sign. Figure 10 shows the turbulent particle flux for the QHS density scan. Above line-averaged density of  $\langle n_e \rangle \sim 2.0 \times 10^{12} \text{ cm}^{-3}$ , the measured particle flux transitions to be directed outward. The Mirror particle flux (not shown) appears to follow the same trend but high enough densities could not be achieved at 0.5 T operation to determine if a similar reversal of measured turbulent particle flux occurs as for QHS plasmas. The fluxes determined from 3D DEGAS neutral gas simulations at two different densities are also shown. From this comparison it appears that the turbulent driven particle flux can account for the anomalously large particle transport determined from neutral gas analysis.

The spectral components of the turbulent particle flux spectra [Eq. (7)] are shown in Fig. 11 for both low ( $1 \times 10^{12} \text{ cm}^{-3}$ ) and high density ( $2.2 \times 10^{12} \text{ cm}^{-3}$ ) discharges in the QHS plasma. The measured particle flux occurs over a broad range of frequencies in both cases. The density-potential cross phase spectra [Fig. 11(c)] are nearly identical, however the measured local poloidal wavenumbers [Fig. 11(b)] reverse sign. This is consistent with the reversal in the direction of the phase velocity observed in Fig. 8. The result is a relative sign change between  $k_\theta - \alpha_{n\Phi}$ , which is responsible for the change in the direction of the particle flux. The change in transport direction is also reflected in the probability distribution function (not shown) where the skewness in  $\Gamma$  changes sign from  $-2$  to  $+2$ . Although the measured turbulent flux direction changes direction, there is no observable change in the characteristic shape of the edge density profile measured by the Thomson scattering.

There are a few sources of ambiguity in the measurement of inward directed particle flux for low-density 0.5 T HSX plasmas. The perturbative nature of the probe measurements has been discussed already. It is likely that the local particle and heat fluxes are modified by the probes acting as

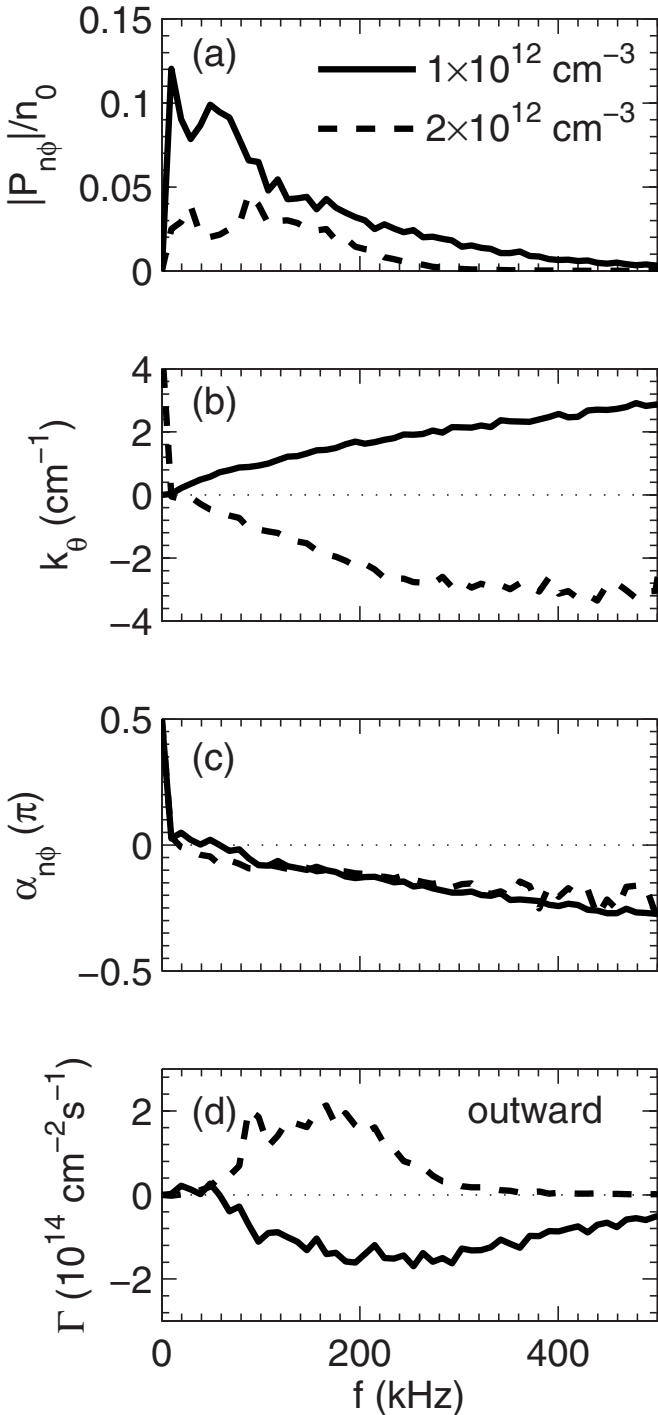


FIG. 11. (a) Amplitude of density-potential cross power spectra, (b) poloidal wavenumber, (c) density-potential cross phase, and (d) transport spectra for lower (solid) and higher (dashed) density QHS discharges.

local sources or sinks of particles and energy. A quantitative analysis of this effect is complicated by the unknown sheath structure surrounding the probe as it is inserted into the plasma.

There is also significant evidence in lower density 0.5 T HSX plasmas for the existence of a suprathermal electron population.<sup>18,19</sup> The spatial distribution of these very energetic electrons (up to many hundred keV) has not yet been measured. Modeling of ECE emission spectra<sup>40</sup> suggests that the distribution is peaked near the ECRH resonance on axis.

However, there could still be a significant number of non-thermal electrons out to the edge plasma, where the probe measurements are being made. These electrons would not be repelled by the negative bias (-300 V) of the ion saturation current measurement, modifying the interpretation of the inferred density. High energy electrons impacting the tungsten tips would also cause secondary electron emission, modifying the floating potential measurement.<sup>32</sup> Based on ECE and soft-X measurements, the population of suprathermal electrons is significantly reduced at the highest densities in 0.5 T plasmas.

The last source of uncertainty results from the neglect of the electron temperature fluctuations in both  $I_{\text{sat}}$  and  $V_{\text{float}}$  measurements. This could modify the overall correlation of the density and potential fluctuations. Significant electron  $T_e$  fluctuations have been measured in the edge of other devices;<sup>41,42</sup> however, the overall impact was not large enough to cause a reversal in the direction of inferred transport.

Although the above mechanisms add uncertainty to the turbulent particle flux interpretation, inward directed particle fluxes have been measured previously in other stellarators. In TJ-II, a change in particle transport direction was attributed to low order rational surfaces, which are also responsible for the triggering of internal transport barriers.<sup>43</sup> In H-1 and compact helical system (CHS) the change from outward to inward directed transport was observed to occur when the measured  $E \times B$  shear rate ( $\omega_E$ ) was larger than a measured decorrelation time scale, estimated as  $V_{\text{phase}}/L_r$ .<sup>44</sup> There are no low order rational surfaces in the QHS and Mirror configurations ( $n,m > 7$ ), but the phase velocities (correlated with the  $E \times B$  velocity) change significantly depending on density (Fig. 8). An  $E \times B$  shear rate can be estimated from the floating potential profiles (ignoring the influence of the  $T_e$  profile), using an expression developed for quasisymmetric stellarators,<sup>45</sup>

$$\omega_E = \frac{k_\perp}{k_\psi} \frac{|\nabla \psi| |\vec{B} \times \nabla \psi|}{B^2} \cdot \left[ (\iota - N) \frac{\partial}{\partial \psi} \left( \frac{1}{(\iota - N)} \frac{\partial}{\partial \psi} \Phi_0(\psi) \right) \right]. \quad (8)$$

Changing variables from  $\psi \rightarrow r$  and using  $k_\perp/k_\psi = 1$  based on the spatial correlation measurements discussed previously, this can be written as

$$\omega_E = \left[ \frac{|\nabla r| |\vec{B} \times \nabla r|}{B^2} B_0 \right] \cdot \frac{1}{B_0} \left| \frac{\partial E_r}{\partial r} + \frac{\iota}{\iota - N} \hat{s} \frac{E_r}{r} \right|, \quad (9)$$

where  $\hat{s} = -r/\iota \cdot \partial \iota / \partial r$  and  $\iota = 1/q$  is the rotational transform. The leading geometry factor varies on a flux surface and has been found using field line integration techniques.<sup>46</sup> In the region of the LFS probe, this factor is about 2.6. Furthermore, in HSX ( $\iota \approx 1.1$ ,  $N=4$ ) the term depending on magnetic shear is negligible ( $\hat{s} \cdot \iota / (\iota - N) < 0.1 \cdot (1/3) \approx 0.03$ ).

Figure 12 shows the floating potential profiles and corresponding  $E \times B$  shear rates from low and high density QHS plasmas. The significant change in the floating potential profiles is consistent with reversal of the  $E \times B$  and phase ve-

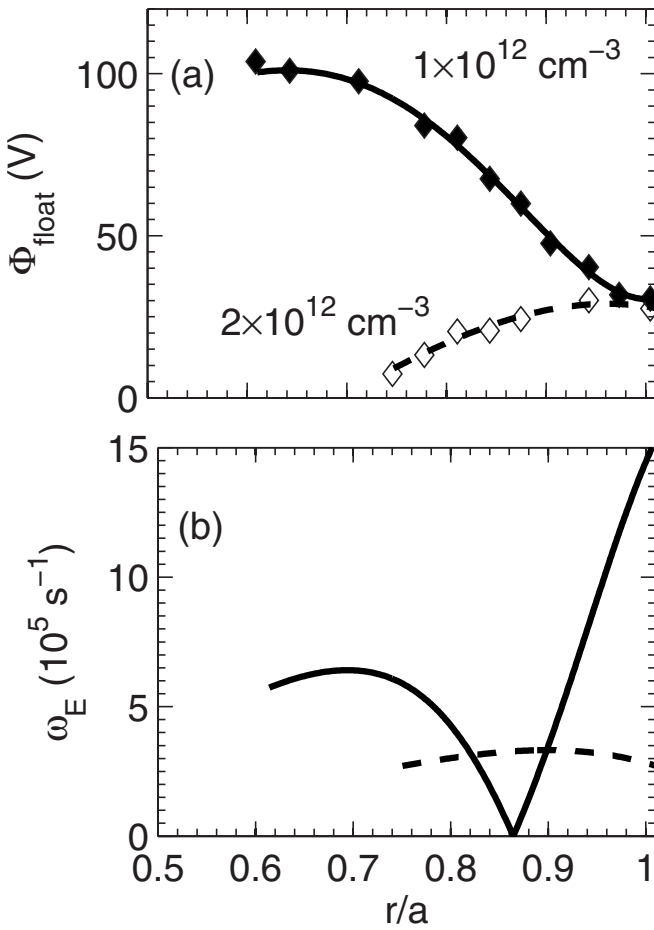


FIG. 12. (a) Floating potential profiles in the low and high density discharges of HSX. (b) Calculated  $E \times B$  shear rates using the floating potential profiles and Eq. (8).

locities in Fig. 8. The calculated shear rates are larger in the lower density discharges over much of the measured edge region. The estimated decorrelation rate  $V_{\text{phase}}/L_r$  for these two cases decreases from  $\sim 8$  to  $5 \times 10^5 \text{ s}^{-1}$ . The observation of inward directed transport in HSX as  $\omega_E$  becomes as large or larger than  $V_{\text{phase}}/L_r$  is consistent with the observations in H-1 and CHS. It is again emphasized, however, that the reversal in measured particle flux does not appear to correspond with any significant changes in the density profiles or overall particle confinement.

#### IV. COMPARISON TO LINEAR DRIFT WAVE THEORY

The measured turbulent particle flux at high density is in good quantitative agreement with the particle flux determined from the neutral gas simulations, as seen in Fig. 10. Given the caveats in the low-density measurements described above, the measurements at high density are mostly focused on from here for making further comparisons to the Weiland model. There are no nonlinear simulations of turbulence in HSX available for comparison to the experimental measurements. Therefore the following comparisons are made to predictions from linear theory.

The Weiland model uses a quasilinear (QL) transport estimate where all quantities are evaluated for a single wavenumber

( $k_\theta \rho_s = 0.3$ ), as it cannot make a prediction for the intensity spectra. The resulting model particle flux can be expressed as a product of a few components, similar to Eq. (7), as

$$\Gamma^{\text{QL}} = n_0 c_s(k_\theta \rho_s) \left| \frac{\delta n}{n_0} \right|^2 \sin(\alpha_{n\Phi}), \quad (10)$$

where  $\delta n/n_0 = e \delta \Phi/T_e$  has been assumed. The density-potential cross phase (along with growth rates and real frequencies) is determined from the solution of the linearized model fluid equations.<sup>6,7</sup> The following comparison focuses on the measured and modeled wavenumber ( $k_\theta \rho_s$ ), intensity ( $\delta n/n_0$ ), cross phase ( $\alpha_{n\Phi}$ ), and transport ( $\Gamma$ ).

As discussed above, the measured transport spectrum peaks around 200 kHz [Fig. 11(d)]. Using the measured dispersion in Fig. 11(b), this corresponds to an average  $\langle k_\theta \rangle \approx 2 \text{ cm}^{-1}$ , or  $\langle k_\theta \rangle \rho_s \approx 0.25$ , which is  $\sim 15\%$  smaller than  $k_\theta \rho_s = 0.3$  prescribed in the evaluation of the Weiland QL transport expression.<sup>6,7</sup> However, the experimental transport is spread over many frequencies and wavenumbers so a quasilinear transport model is neglecting a significant amount of information.

The predicted phase velocities from the Weiland model are  $\sim 1.2 \text{ km/s}$ , much smaller than the measured phase velocities ( $\sim 5 \text{ km/s}$ , Fig. 8) in the laboratory frame. Uncertainty in the  $E \times B$  Doppler shift would need to be reduced considerably to confirm a direction of propagation.

The dashed line in Fig. 3 shows the mixing length estimate as used in the Weiland model, given by

$$\left( \frac{\delta n}{n_0} \right)^{\text{ML}} = \frac{\gamma}{\omega_{*e} k_\theta L_n} \frac{1}{k_\theta}, \quad (11)$$

where  $\omega_{*e} = k_\theta T_e / BL_n$  and  $k_\theta = k_r$  is assumed. It is apparent that these values underestimate the measured values in the outer region of the plasma by  $\sim 50\%$ . The ratio of linear growth rate to real frequency in Eq. (11) often approaches unity. The corresponding difference in Eq. (11) and the measurements in Fig. 3 is consistent with the difference in measured radial correlation length ( $\sim 7 \rho_s$ ) and the corresponding model “correlation length,”  $\gamma/\omega_{*e} k_\theta \approx 2-4 \rho_s$ .

It is interesting to note that the comparison between LFS and HFS probes indicates that the measured turbulence does not exhibit a strong ballooning character. Figure 13 shows the fluctuation intensity in the QHS configuration on the LFS is at most 25% larger than the HFS ( $\delta n^{\text{LFS}} / \delta n^{\text{HFS}} \approx 1.25$ ). While a stronger ballooning character has been observed in some tokamak edge probe measurements,<sup>47</sup> linear eigenmodes from global 3D gyrokinetic stability analysis in HSX (Ref. 22) are not that strongly ballooning ( $\delta n^{\text{LFS}} / \delta n^{\text{HFS}} \approx 1.5$ ), consistent with the turbulence measurements here. However, the calculations in Ref. 22 were performed for the ITG instability with adiabatic electrons so the TEM instability is not treated.

From the multiple turbulence measurements, the density-potential cross phase spectra,  $\alpha_{n\varphi}(f)$ , and local poloidal wavenumber spectra,  $k_\theta(f)$ , have been used to create a power spectrum weighted,  $k_\theta \alpha_{n\varphi}$  spectra,

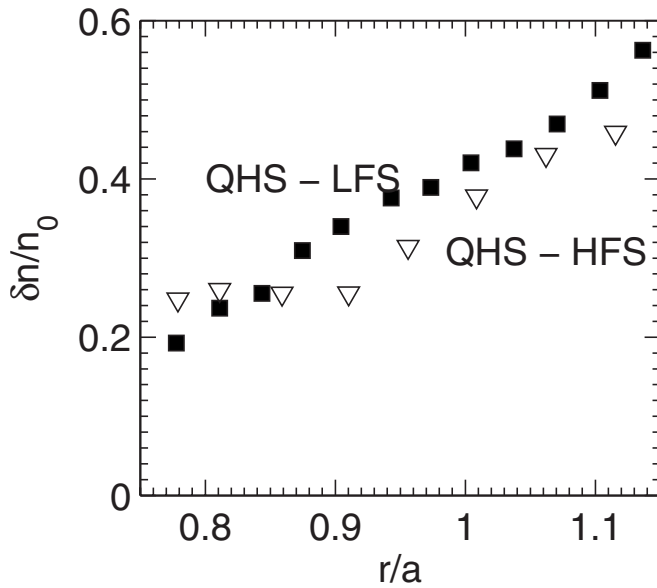


FIG. 13. Normalized  $I_{\text{cat}}$  fluctuation levels measured in the QHS configuration for both LFS and HFS probes.

$$\hat{S}(k_\theta, \alpha_{n\varphi}) = \frac{\int_f P(k_\theta, \alpha_{n\varphi} | f) S(k_\theta, \alpha_{n\varphi} | f)}{\int_f S(k_\theta, \alpha_{n\varphi} | f)}, \quad (12)$$

where  $P(k_\theta, \alpha_{n\varphi} | f)$  and  $S(k_\theta, \alpha_{n\varphi} | f)$  are the joint distribution function and power spectrum of  $k_\theta, \alpha_{n\varphi}$ , conditioned on frequency. When negative wavenumbers are calculated, the signs of both  $k_\theta$  and  $\alpha_{n\varphi}$  are changed. This results in positive definite wavenumbers with the correct relative sign between  $k_\theta, \alpha_{n\varphi}$ , which maintains the correct transport direction. Average and standard deviations of the cross phase are then calculated at each wavenumber. Figure 14 shows the mean spectrum-averaged  $n\varphi$  cross phase, along with lines representing the standard deviation of the distribution. These represent the width of the distribution of the measured cross phase and are not an uncertainty estimate.

For a given wavenumber, the cross phases are distributed over a very broad range, indicative of the strong turbulence present. The mean cross phase reaches values as large as  $\sim 30^\circ$  near  $k_\theta \rho_s \approx 0.4 - 0.6$ , and approaches zero at  $k_\theta \rho_s = 0$ . This is consistent with drift waves as they are linearly stable at  $k_\theta \rho_s = 0$ . Above the values of  $k_\theta \rho_s \approx 0.5 - 0.6$  on Fig. 14, the coherency between the signals used to infer  $k_\theta$  and  $\alpha_{n\varphi}$  is dropping significantly, reducing the significance of the derived spectra in that region. Also shown in Fig. 14 is the theoretically calculated  $n\varphi$  cross phase from the Weiland model. The predicted linear cross phases are consistently higher ( $\sim 15^\circ - 20^\circ$ ) than the mean experimental cross phases, but are well within one-sigma ( $\sim 30^\circ - 45^\circ$ ) of the measured turbulent distribution of cross phases.

There is some evidence from gyrokinetic simulations of TEM turbulence in tokamak geometry that the mean  $n\varphi$  cross phases in the nonlinear turbulent state are nearly identical to the linear cross phases.<sup>48</sup> However, fluid simulations exist where the nonlinear structure of the turbulence can

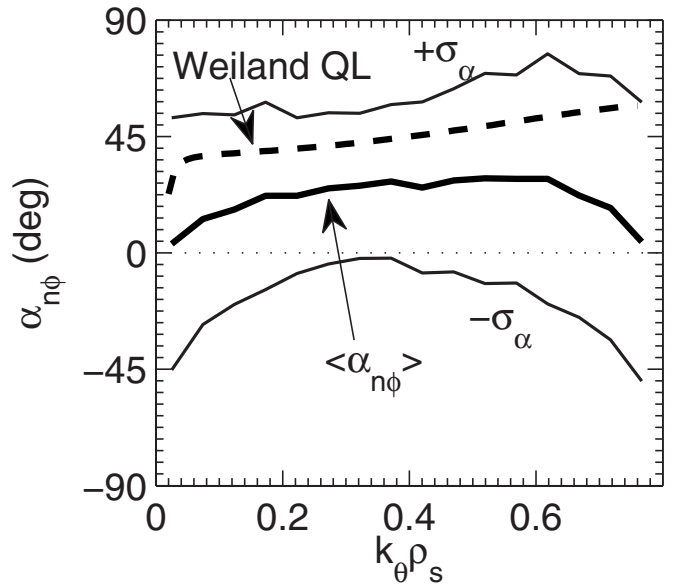


FIG. 14. Measured mean density-potential cross phase vs local poloidal wavenumber. The thin lines represent the standard deviation of the measured  $n\varphi$  cross phase. Also shown is the  $n\varphi$  cross phase from the Weiland linear stability calculation.

differ substantially from the linear predictions.<sup>49</sup> Nonlinear simulations would be required, using the HSX stellarator geometry with appropriate experimental plasma parameters, to determine whether the above measured distribution of cross phases is consistent with TEM turbulence.

The resulting transport prediction from the Weiland model (shown in Fig. 10) is three to four times smaller than the flux inferred from the Langmuir probe measurements and DEGAS results. This difference is nearly consistent with the cumulative differences in the wavenumber ( $\sim 0.8$ ), intensity ( $\sim 2^2 = 4$ ), and cross phases ( $\sim 0.7$ ) discussed above in the context of Eq. (10)  $\{(0.25/0.3)(2)^2[\sin(30^\circ)/\sin(40^\circ)] \sim 2.5\}$ .

While prone to increased uncertainty, higher order spectral calculations have been used to infer growth rates from turbulence measurements.<sup>50,51</sup> Bispectral analysis<sup>52</sup> can be used to measure the rate of energy transfer between fluctuating wave components due to nonlinear three-wave interactions that satisfy  $\vec{k} = \vec{k}_1 + \vec{k}_2$ . Assuming the evolution of a turbulent spectrum can be modeled using only quadratic (three-wave) processes, a single field model equation can be written,<sup>50</sup>

$$\frac{\partial \varphi_k}{\partial t} = \Lambda_k^L \varphi_k + \sum_{k=k_1+k_2} \Lambda_{k_1, k_2}^Q \varphi_{k_1} \varphi_{k_2}, \quad (13)$$

where  $\Lambda_{k_1, k_2}^{L, Q}$  are the linear and nonlinear transfer functions. If the turbulence is statistically stationary, the nonlinear energy transfer is assumed to be balanced by the linear growth of the instabilities. With this assumption a set of equations can be derived<sup>50,51</sup> to determine an experimental estimate of the growth rate spectrum using the measured power spectra

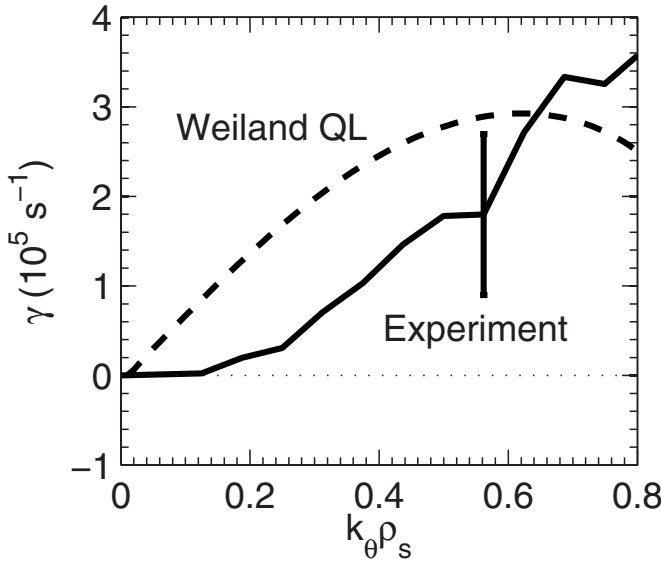


FIG. 15. Experimentally inferred growth rates for the high density QHS discharge ( $r/a=0.8$ ). Also shown is the linear prediction from the Weiland model.

$\langle \varphi_k^1 \varphi_k^{1*} \rangle$ , cross spectra  $\langle \varphi_k^1 \varphi_k^{2*} \rangle$ , and bispectra  $\langle \varphi_{k1}^1 \varphi_{k2}^1 \varphi_{k3}^{2*} \rangle$ , where  $\langle \dots \rangle$  represents an ensemble average and the superscript numbers represent measurements at two points in time to approximate a finite difference of  $\partial \varphi_k / \partial t$ .

Ideally, this method would use time dependent wave-number spectra  $[\varphi(\vec{k}, t)]$ , which is usually not feasible to measure. It is much easier to measure space dependent frequency spectra  $[\varphi(f, \vec{x})]$ , as has been done in the above experiments. These measurements can still be used in the bispectral analysis as the fluctuations are moving rapidly past the observation points. With phase velocities on the order of 5–10 km/s, the turbulence is propagating by the two floating potential measurements in a time ( $\sim 0.6$ – $1.3$   $\mu$ s) faster than a typical decorrelation time (3–5  $\mu$ s). Therefore Taylor's “frozen flow” hypothesis can be used to transform between wavenumber and frequency space, via  $k_\theta = \omega / V_{\text{phase}}$ .

The above analysis (see Ref. 51) has been performed for the higher density QHS plasma using the poloidally separated floating potential measurements. The resulting inferred growth rate spectrum is shown in Fig. 15. About 1500 independent time series have been used from similar discharges to reduce statistical uncertainty in the bispectrum estimators. The uncertainty estimate shown in the figure was found using a Monte Carlo approach assuming 10% random noise of both amplitude and phase of the measured frequency spectra. This likely underestimates the true uncertainty at higher frequency (wavenumber) as it does not account for the reduction in overall coherence and bicoherence of the measured signals above  $k_\theta \rho_s \approx 0.5$ .

The inferred growth rates are on the order of a few  $10^5$   $\text{s}^{-1}$  (consistent with the decorrelation rates, validating Taylor's hypothesis) and approach zero at  $k_\theta \rho_s = 0$ , consistent with drift waves which are linearly stable. Also shown is the predicted linear growth rate spectrum from the Weiland

model for the same case shown in Fig. 14. The agreement in the predicted and measured growth rates is comparable to that in the density-potential cross phase.

The predicted and experimentally inferred growth rates in Fig. 15 appear to peak at values of  $k_\theta \rho_s \approx 0.5$  or greater. However the peak in transport is estimated to occur at the smaller values of  $k_\theta \rho_s \approx 0.25$  or 0.3. This downshift in peak spectra is often observed in magnetically confined plasmas due to the inverse cascade expected in two-dimensional turbulence.<sup>53</sup>

## V. SUMMARY

Langmuir probes have been used in ECRH  $B=0.5$  T plasmas in HSX to characterize the edge ( $r/a=0.8$ – $1.0$ ) turbulence. It is found that the measured turbulent particle transport does indeed account for the anomalous transport determined from 1D analysis using neutral gas simulations. The measured turbulence intensities in electron-heated  $B=0.5$  T HSX plasmas are strong ( $\delta n / n_0 \sim e \delta \Phi / T_e \sim 10\%-40\%$ ) with fluctuations existing over a broad range of frequencies and wavenumbers. Correlation lengths are isotropic and follow the local gyroradius ( $\langle \Delta k_\theta \rangle^{-1} \sim L_r \sim 7 \rho_s$ ), consistent with local (gyro-Bohm) drift wave expectations. In addition, measurements at two different locations indicate the turbulence is not strongly ballooning. The edge turbulence is very similar for plasmas in both the optimized (QHS) and nonoptimized (Mirror) configurations.

While the above features are generally consistent with drift wave expectations, a quantitative comparison has been made between the turbulence characteristics and the Weiland quasilinear TEM drift wave model that has previously been used to predict the anomalous transport in HSX.<sup>28</sup> The measured density-potential cross phases are  $\sim 30\%$  smaller than the linear TEM predictions, but are well within one standard deviation of the measured distribution. The measured intensities are approximately two times larger than the model mixing length estimate, and the overall measured transport is approximately three to four times larger than the resulting model transport prediction. The low level of model transport results mostly from the inadequacy of the simple mixing length estimate.

The discrepancy in measured and modeled transport in these  $B=0.5$  T plasmas is quantitatively consistent with that seen in the edge of the  $B=1.0$  T predictions in Ref. 28. There, the modeled flux (diffusivity), using measured profiles as input, was outside experimental uncertainties for most of the profile. However, when using experimental sources as input, the predicted profiles were within experimental uncertainties due to the sensitivity of model transport with respect to driving gradients. For a more thorough validation,<sup>10</sup> future work should test the sensitivity of this (and other) model predictions with the turbulence and transport measurements within experimental uncertainties. It is also hoped that future comparisons can be made with more comprehensive nonlinear 3D gyrokinetic simulations that are becoming available (e.g., Refs. 25 and 26). Specifically, a comparison of more detailed measurements for both the

QHS and Mirror configurations with such simulations will hopefully lead to a better understanding of the influence of the 3D geometry on the turbulent transport.

## ACKNOWLEDGMENTS

The authors would like to thank Stefan Gerhardt, Carsten Lechte, Jeremy Lore, Mike Frankowski, Tony Piccione, and Paul Probert for their assistance, and Jim Callen, Chris Hegna, and Paul Terry for many useful discussions.

This work was supported by the U.S. Department of Energy under Contract No. DE-FG02-93ER54222.

- <sup>1</sup>ITER Physics Basis editors, *Nucl. Fusion* **39**, 2175 (1999).
- <sup>2</sup>E. J. Doyle, W. A. Houlberg, Y. Kamada, V. Mukhovatov, T. H. Osborne, A. Polevoi, G. Bateman, J. W. Connor, J. G. Cordey, T. Fujita, X. Garbet, T. S. Hahm, L. D. Horton, A. E. Hubbard, F. Imbeaux, F. Jenko, J. E. Kinsey, Y. Kishimoto, J. Li, T. C. Luce, Y. Martin, M. Ossipenko, V. Parail, A. Peeters, T. L. Rhodes, J. E. Rice, C. M. Roach, V. Rozhansky, F. Ryter, G. Saibene, R. Sartori, A. C. C. Sips, J. A. Snipes, M. Sugihara, E. J. Synakowski, H. Takenaga, T. Takizuka, K. Thomsen, M. R. Wade, H. R. Wilson, ITPA Transport Physics Topical Group, ITPA Confinement Database and Modelling Topical Group, and ITPA Pedestal and Edge Topical Group, *Nucl. Fusion* **47**, S18 (2007).
- <sup>3</sup>U. Stroth, *Plasma Phys. Controlled Fusion* **40**, 9 (1998).
- <sup>4</sup>F. Wagner and U. Stroth, *Plasma Phys. Controlled Fusion* **35**, 1321 (1993).
- <sup>5</sup>J. Candy and R. E. Waltz, *Phys. Rev. Lett.* **91**, 045001 (2003).
- <sup>6</sup>H. Nordman, J. Weiland, and A. Jarmén, *Nucl. Fusion* **30**, 983 (1990).
- <sup>7</sup>G. Bateman, A. H. Kritz, J. E. Kinsey, A. J. Redd, and J. Weiland, *Phys. Plasmas* **5**, 1793 (1998).
- <sup>8</sup>M. Kotschenreuther, W. Dorland, G. W. Hammett, and M. A. Beer, *Phys. Plasmas* **2**, 2381 (1995).
- <sup>9</sup>R. E. Waltz, G. W. Staebler, W. Dorland, G. W. Hammett, M. Kotschenreuther, and J. A. Konings, *Phys. Plasmas* **4**, 2482 (1997).
- <sup>10</sup>P. W. Terry, M. Greenwald, J.-N. Leboeuf, G. R. McKee, D. R. Mikkelsen, W. M. Nevins, D. E. Newman, D. P. Stotler, Task Group on Verification and Validation, U.S. Burning Plasma Organization, and U.S. Transport Task Force, *Phys. Plasmas* **15**, 062503 (2008).
- <sup>11</sup>D. W. Ross R. V. Bravenec, W. Dorland, M. A. Beer, and G. W. Hammett, *Phys. Plasmas* **9**, 177 (2002); D. W. Ross and W. D. Dorland, *ibid.* **9**, 5031 (2002).
- <sup>12</sup>A. E. White, L. Schmitz, G. R. McKee, C. Holland, W. A. Peebles, T. A. Carter, M. W. Shafer, M. E. Austin, K. H. Burrell, J. Candy, J. C. DeBoo, E. J. Doyle, M. A. Makowski, R. Prater, T. L. Rhodes, G. M. Staebler, G. R. Tynan, R. E. Waltz, and G. Wang, *Phys. Plasmas* **15**, 056116 (2008).
- <sup>13</sup>L. Lin, M. Porkolab, E. M. Edlund, J. C. Rost, C. L. Fiore, M. Greenwald, Y. Lin, D. R. Mikkelsen, N. Tsujii, and S. J. Wukitch, *Phys. Plasmas* **16**, 012502 (2009).
- <sup>14</sup>H. E. Myrick, *Phys. Plasmas* **13**, 058102 (2006).
- <sup>15</sup>F. S. B. Anderson, D. T. Anderson, A. Almagri, P. G. Matthews, J. N. Talmadge, and J. L. Shohet, *Fusion Technol.* **27**, 273 (1995).
- <sup>16</sup>J. Nuhrenberg and R. Zille, *Phys. Lett. A* **129**, 113 (1988).
- <sup>17</sup>S. P. Gerhardt, J. N. Talmadge, J. M. Canik, and D. T. Anderson, *Phys. Rev. Lett.* **94**, 015002 (2005); *Phys. Plasmas* **12**, 056116 (2005).
- <sup>18</sup>J. N. Talmadge, F. S. B. Anderson, D. T. Anderson, C. Deng, W. Guttenfelder, K. M. Likin, J. Lore, J. C. Schmitt, and K. Zhai, *J. Plasma Fusion Res.* **3**, S1002 (2008).
- <sup>19</sup>J. M. Canik, D. T. Anderson, F. S. B. Anderson, K. M. Likin, J. N. Talmadge, and K. Zhai, *Phys. Rev. Lett.* **98**, 085002 (2007); *Phys. Plasmas* **14**, 056107 (2007).
- <sup>20</sup>F. Wagner, S. Bäumel, J. Baldzuhn, N. Basse, R. Brakel, R. Burhenn, A. Dinklage, D. Dorst, H. Ehmler, M. Endler, V. Erckmann, Y. Feng, F. Gadelmeier, J. Geiger, L. Giannone, P. Grigull, H.-J. Hartfuss, D. Hartmann, D. Hildebrandt, M. Hirsch, E. Holzhauer, Y. Igitkhanov, R. Jänicke, M. Kick, A. Kislyakov, J. Kisslinger, T. Klinger, S. Klose, J. P. Knauer, R. König, G. Kühner, H. P. Laqua, H. Maassberg, K. McCormick, H. Niedermeyer, C. Nührenberg, E. Pasch, N. Ramasubramanian, N. Ruhs, N. Rust, E. Sallander, F. Sardei, M. Schubert, E. Speth, H. Thomsen, F. Volpe, A. Weller, A. Werner, H. Wobig, E. Würsching, M. Zarnstorff, and S. Zoletnik, *Phys. Plasmas* **12**, 072509 (2005).
- <sup>21</sup>O. Motojima, N. Ohayabu, A. Komori, O. Kaneko, H. Yamada, K. Kawahata, Y. Nakamura, K. Ida, T. Akiyama, N. Ashikawa, W. A. Cooper, A. Ejiri, M. Emoto, N. Ezumi, H. Funaba, A. Fukuyama, P. Goncharov, M. Goto, H. Idei, K. Ikeda, S. Inagaki, M. Isobe, S. Kado, H. Kawazome, K. Khlopov, T. Kobuchi, K. Kondo, A. Kostrioukov, S. Kubo, R. Kumazawa, Y. Liang, J. F. Lyon, A. Mase, S. Masuzaki, T. Minami, J. Miyazawa, T. Morisaki, S. Morita, S. Murakami, S. Muto, T. Mutoh, K. Nagaoka, Y. Nagayama, N. Nakajima, K. Nakamura, H. Nakanishi, K. Narihara, Y. Narushima, K. Nishimura, N. Nishino, N. Noda, T. Notake, H. Nozato, S. Ohdachi, Y. Oka, H. Okada, S. Okamura, M. Osakabe, T. Ozaki, B. J. Peterson, A. Sagara, T. Saida, K. Saito, S. Sakakibara, M. Sakamoto, R. Sakamoto, M. Sasao, K. Sato, M. Sato, T. Seki, T. Shimozuma, M. Shoji, H. Suzuki, Y. Takeiri, N. Takeuchi, N. Tamura, K. Tanaka, M. Y. Tanaka, Y. Teramachi, K. Toi, T. Tokuzawa, Y. Tomota, Y. Torii, K. Tsumori, K. Y. Watanabe, T. Watari, Y. Xu, I. Yamada, S. Yamamoto, T. Yamamoto, M. Yokoyama, S. Yoshimura, Y. Yoshimura, M. Yoshinuma, N. Asakura, T. Fujita, T. Fukuda, T. Hatae, S. Higashijima, A. Isayama, Y. Kamada, H. Kubo, Y. Kusama, Y. Miura, T. Nakano, H. Ni-nomiya, T. Oikawa, N. Oyama, Y. Sakamoto, K. Shinohara, T. Suzuki, H. Takenaga, K. Ushigusa, T. Hino, M. Ichimura, Y. Takase, F. Sano, H. Zushi, T. Satow, S. Imagawa, T. Mito, I. Ohtake, T. Uda, K. Itoh, K. Ohkubo, S. Sudo, K. Yamazaki, K. Matsuoka, Y. Hamada, and M. Fujiwara, *Nucl. Fusion* **43**, 1674 (2003).
- <sup>22</sup>G. Jost, T. M. Tran, W. A. Cooper, L. Villard, and K. Appert, *Phys. Plasmas* **8**, 3321 (2001).
- <sup>23</sup>F. Jenko and A. Kendt, *Phys. Plasmas* **9**, 4103 (2002).
- <sup>24</sup>G. Rewoldt, L.-P. Ku, and W. M. Tang, *Phys. Plasmas* **12**, 102512 (2005).
- <sup>25</sup>P. Xanthopoulos, F. Merz, T. Görler, and F. Jenko, *Phys. Rev. Lett.* **99**, 035002 (2007).
- <sup>26</sup>T.-H. Watanabe, H. Sugama, and S. Ferrando-Margalet, *Phys. Rev. Lett.* **100**, 195002 (2008).
- <sup>27</sup>O. Yamagishi, M. Yokoyama, N. Nakajima, and K. Tanaka, *Phys. Plasmas* **14**, 012505 (2007).
- <sup>28</sup>W. Guttenfelder, J. Lore, D. T. Anderson, F. S. B. Anderson, J. M. Canik, W. Dorland, and J. N. Talmadge, *Phys. Rev. Lett.* **101**, 215002 (2008).
- <sup>29</sup>K. M. Likin, A. Abdou, A. F. Almagri, D. T. Anderson, F. S. B. Anderson, D. Brower, J. Canik, C. Deng, S. P. Gerhardt, W. Guttenfelder, S. Oh, J. Radler, V. Sakaguchi, J. Schmitt, J. Tabora, J. N. Talmadge, and K. Zhai, *Plasma Phys. Controlled Fusion* **45**, A133 (2003).
- <sup>30</sup>K. Zhai, F. S. B. Anderson, K. Willis, K. Likin, and D. T. Anderson, *Rev. Sci. Instrum.* **75**, 3900 (2004).
- <sup>31</sup>C. Deng, D. L. Brower, W. X. Deng, A. F. Almagri, D. T. Anderson, F. S. B. Anderson, S. P. Gerhardt, P. Probert, and J. N. Talmadge, *Rev. Sci. Instrum.* **74**, 1625 (2003).
- <sup>32</sup>N. Hershkowitz, *Plasma Diagnostics* (Academic, Boston, 1989), Vol. 1, p. 113.
- <sup>33</sup>P. Liewer, *Nucl. Fusion* **25**, 543 (1985).
- <sup>34</sup>A. J. Wooton, B. A. Carreras, H. Matsumoto, K. McGuire, W. A. Peebles, Ch. P. Ritz, P. W. Terry, and S. J. Zweben, *Phys. Fluids B* **2**, 2879 (1990).
- <sup>35</sup>G. D. Conway, *Plasma Phys. Controlled Fusion* **50**, 124026 (2008).
- <sup>36</sup>J. M. Beall, Y. C. Kim, and E. J. Powers, *J. Appl. Phys.* **43**, 3993 (1982).
- <sup>37</sup>S. J. Levinson, J. M. Beall, E. J. Powers, and R. D. Bengtson, *Nucl. Fusion* **24**, 527 (1984).
- <sup>38</sup>E. J. Powers, *Nucl. Fusion* **14**, 749 (1974).
- <sup>39</sup>D. B. Heifetz, D. Post, M. Petracic, J. Weisheit, and G. Bateman, *J. Comput. Phys.* **46**, 309 (1982).
- <sup>40</sup>K. M. Likin, A. F. Almagri, D. T. Anderson, F. S. B. Anderson, C. Deng, H. Lu, J. Radler, J. N. Talmadge, and K. Zhai, *Bull. Am. Phys. Soc.* **49**, 307 (2004).
- <sup>41</sup>H. Lin, R. D. Bengtson, and Ch. P. Ritz, *Phys. Fluids B* **1**, 2027 (1989).
- <sup>42</sup>P. C. Liewer, J. M. McChesney, S. J. Zweben, and R. W. Gould, *Phys. Fluids* **29**, 309 (1986).
- <sup>43</sup>M. A. Pedrosa, C. Hidalgo, D. López-Bruna, A. López-Fragua, J. Castellano, and J. A. Jiménez, *Plasma Phys. Controlled Fusion* **43**, 1573 (2001).
- <sup>44</sup>M. G. Shats, K. Toi, K. Ohkuni, Y. Yoshimura, M. Osakabe, G. Matsunaga, M. Isobe, S. Nishimura, S. Okamura, K. Matsuoka, and C. H. S. Group, *Phys. Rev. Lett.* **84**, 6042 (2000).
- <sup>45</sup>T. S. Hahm, *Phys. Plasmas* **4**, 4074 (1997).
- <sup>46</sup>V. V. Nemov, *Nucl. Fusion* **28**, 1727 (1988).

- <sup>47</sup>B. LaBombard, J. E. Rice, A. E. Hubbard, J. W. Hughes, M. Greenwald, R. S. Granetz, J. H. Irby, Y. Lin, B. Lipschultz, E. S. Marmar, K. Marr, D. Mossessian, R. Parker, W. Rowan, N. Smick, J. A. Snipes, J. L. Terry, S. M. Wolfe, and S. J. Wukitch, *Phys. Plasmas* **12**, 056111 (2005).
- <sup>48</sup>T. Dannert and F. Jenko, *Phys. Plasmas* **12**, 072309 (2005).
- <sup>49</sup>B. D. Scott, *Phys. Plasmas* **12**, 062314 (2005).
- <sup>50</sup>Ch. P. Ritz, E. J. Powers, and R. D. Bengtson, *Phys. Fluids B* **1**, 153 (1989).
- <sup>51</sup>J. S. Kim, R. D. Durst, R. J. Fonck, E. Fernandez, A. Ware, and P. W. Terry, *Phys. Plasmas* **3**, 3998 (1996).
- <sup>52</sup>Y. C. Kim and E. J. Powers, *IEEE Trans. Plasma Sci.* **PS-7**, 120 (1979).
- <sup>53</sup>R. H. Kraichnan, *Phys. Fluids* **10**, 1417 (1967).